Optimizing water demand in citrus orchards: a novel model using evolutionary algorithms on Sentinel-1 time series data

Emilio-José Cabello-Franco, Daniel Antón, Emilio Ramírez-Juidias & Francisco Perea-Torres

Published online: 13 Aug 2025.

Submit your article to this journal ↗

Article views: 220

View related articles ↗

View Crossmark data ↗

co:gent

SOIL & CROP SCIENCES | RESEARCH ARTICLE

🔓 OPEN ACCESS   🔄 Check for updates

Optimizing water demand in citrus orchards: a novel model using evolutionary algorithms on Sentinel-1 time series data

Emilio-José Cabello-Franco[a] 🆔, Daniel Antón[b,c] 🆔, Emilio Ramírez-Juidias[d] 🆔 and Francisco Perea-Torres[e] 🆔

[a]RSV3 Remote Sensing S.L., Sanlucar La Mayor, Seville, Spain; [b]Departamento de Expresión Gráfica e Ingeniería en la Edificación, Escuela Técnica Superior de Ingeniería de Edificación, Universidad de Sevilla, Seville, Spain; [c]Product Innovation Centre and The Creative and Virtual Technologies Research Lab, School of Architecture, Design and the Built Environment, Nottingham Trent University, Nottingham, UK; [d]Instituto Universitario de Arquitectura y Ciencias de la Construcción (IUACC), Universidad de Sevilla, Seville, Spain; [e]Andalusian Institute of Agricultural and Fisheries Research and Training (IFAPA), Center Las Torres, Seville, Spain

ABSTRACT

Citrus fruits are crucial globally, impacting economies and livelihoods. However, climate change is affecting water availability and usage, posing challenges for managing water in citrus crops. This paper introduces CARP-flux, a new model designed to assess water needs in citrus orchards, specifically addressing the limitations of traditional methods under changing climates. The study was conducted in El Hundido, an irrigation village located in the Vega del Guadalquivir Valley near Cantillana, Seville (Spain), acknowledged as a significant citrus trade area at both the European and national levels. To adjust the model to contemporary climate conditions, time-series data from the Sentinel-1 Interferometric Wide (IW) satellite (VV and VH polarizations) from 2021 and 2022 were employed. Employing genetic algorithms and the Weibull distribution, the study incorporated 3D radiation models from backscatter data, a spatial interpretation of water and radiation dynamics, which, in turn, validated CARP-flux's performance. This model proved effective in identifying land-use changes and evaluating radiation intensity, which are critical factors for understanding crop water needs in climate change scenarios. CARP-flux offers a precise alternative to the conventional Hargreaves technique for citrus groves, which underestimates water requirements in irrigated and humid regions with ample soil moisture, such as the Vega del Guadalquivir.

1. Introduction

To monitor the condition and performance of citrus orchards using satellite remote sensing, image time series should be of high spatial and temporal resolution. Similarly, ground campaigns should cover the full crop cycle, including regular data collection over the full study area. According to Vidican et al. (2023), the growing number of satellites and the accessibility of free data have offered new possibilities for land cover and crop type classification through the integration of multi-sensor images in coherent time series. To achieve this, considering the revisit time of the satellites used is crucial. Sentinel-1 operates in a near-polar, sun-synchronous orbit, repeating its path every 12 days and completing 175 orbits per cycle for one satellite. Sentinel-1A and Sentinel-1B are in the same orbital plane but are phased 180° apart. When both satellites are active, the repeat cycle is reduced to six days (ESA, 2024a, 2024b). Sentinel-2A and Sentinel-2B satellites, also sun-synchronous, are spaced 180 degrees apart and revisit all areas every five days under identical viewing conditions. The overlap between swaths from adjacent orbits increases the revisit frequency but with different viewing conditions (ESA, 2024b). The joint use of Sentinel-1 and Sentinel-2 allows for improved identification of various growth cycle stages that are often difficult to perceive when relying on infrequent data (Vidican et al., 2023).

Research has integrated optical and microwave images to enhance the precision of mapping in agricultural settings (Adrian et al., 2021; Frau Orynbaikyzy, 2023; Komisarenko et al., 2022; Kpienbaareh et al., 2021; Shrestha et al., 2021; Tufail et al., 2022). Synthetic Aperture Radar (SAR) data are not affected by the amount of sunlight but by the wavelength, roughness, geometry, and material composition of the surface being observed. By contrast, optical data are significantly impacted by cloud cover and depict the amount of solar radiation reflected from a specific area. Remote sensing for land and water resource administration has also been used (Ellis et al., 2024; Food & Agriculture Organization of the United Nations (FAO), 2024). The ability to regularly observe, combined with high-resolution multispectral data, enables accurate and cost-effective mapping of citrus orchards and irrigated areas (Jovanovic et al., 2020).

Crop water demand refers to the amount of water required to compensate for water lost (to the atmosphere) through evapotranspiration in a cropped field, and it is a fundamental aspect of both agronomy and environmental science. In citrus orchards, it varies depending on growth stage and plot location. The FAO Penman-Monteith approach (Allen et al., 1998; Allen et al., 2007a, 2007b); Bastiaanssen et al., 1998), defines and calculates the reference evapotranspiration (ET_o). From crop surfaces under typical conditions, crop evapotranspiration (ET_c) is based on crop coefficients (K_c) that establish the relationship between ET_c and ET_o. The dual crop coefficient approach divides K_c into two distinct coefficients: one for crop transpiration (K_{cb}, basal crop coefficient) and another for soil evaporation (K_e).

Remote sensing contributes to estimating crop evapotranspiration by leveraging vegetation reflecting features and the correlation between evapotranspiration and crop attributes such as the Leaf Area Index (LAI) and crop coefficient (K_c). ET_c can be computed from remote sensing data by physics-based approaches that rely on the surface energy balance (Allen et al., 2007b, 2007a; Bastiaanssen et al., 1998; Friedman, 2024; Sahaar et al., 2022), or through empirical methods that utilize vegetation indicators (Dari et al., 2020; De Michele et al., 2020; El Hajj et al., 2023; Jovanovic et al., 2020; Osann Jochum, 2006). Physics-based techniques are used to estimate the transfer of latent heat through the surface energy balance. However, the challenges associated with measuring its components have resulted in a greater reliance on empirical methods, which determine the crop coefficient using the vegetation indices methodology. ET_c estimation using vegetation indices, often the Normalized Difference Vegetation Index (NDVI), is a modified version of the crop coefficients approach (Doorenbos & Pruitt, 1977; Pereira & Allen, 1999). According to Salgado and Mateos (2021), ET_o is derived using meteorological data, and K_c incorporates information specific to the studied crop. These methods frequently rely on tabular values to obtain crop data, which offer broad information for multiple crops (Allen et al., 2007b, 1998; Bastiaanssen et al., 1998). To enhance the precision of estimating crop water requirements, the K_c curves must be characterized. This can be achieved by utilizing remote sensing data, as there is a strong correlation between crop attributes and spectral reflectances (Pôças et al., 2020; Steduto et al., 2012). Therefore, the K_c-NDVI technique establishes a practical connection between K_c values obtained through field measurements and NDVI values extracted from remote sensing optical data (Dari et al., 2020; De Michele et al., 2020; El Hajj et al., 2023; Jovanovic et al., 2020; Osann Jochum, 2006). Once calibrated and validated for a specific area, the equations for estimating K_c values based on vegetation indices can provide accurate estimates of ET_c (Jovanovic et al., 2020; Pôças et al., 2020; Steduto et al., 2012).

This study proposes a genetic algorithm-based flux model, CARP-flux, to estimate water requirements in citrus orchards using Sentinel-1 radar satellite imagery. Time series from multiple orbital directions are employed to achieve high spatial (10 m) and temporal (daily to 3–5 days) resolution. This enables the evaluation of orchard conditions through Vegetation Indices (VIs) and VV + VH backscatter data.

To validate the CARP-flux model, an ad hoc method was developed to generate 3D radiation data from Sentinel-1 imagery. This spatial representation of 2D radar backscatter enables the characterization of soil moisture, detection of land use changes, and estimation of both fruit quality and grower practices. The method consists of automated image segmentation and conversion into 3D point clouds, allowing qualitative and quantitative analysis of backscatter behavior via histograms and statistical metrics.

Overall, this research lays the groundwork for estimating water requirements in citrus orchards using evolutionary algorithms based solely on radar satellite data.

2. Materials and methods

2.1. Study area

This research was conducted at the El Hundido community of irrigators, located within the larger irrigation area of the same name (Figure 1). The El Hundido community is on the right bank of the Guadalquivir River, immediately upstream of its confluence with the Viar River, in the municipality of Cantillana in Seville (Andalusia, Spain).

Both rivers and the urban center of Cantillana delimit the area. Its perimeter is indicated in Figure 1 in red color with its centroid 'C', whose coordinates, 37.59458°N, 5.84059°W, are also specified in the caption of subsequent satellite images of the study area. The coordinates of the boundary polygon's vertex with the lowest latitude and longitude (i.e. the southwesternmost point) are 37.585497° N, 5.861256° W.

Most of the irrigated surface (270 hectares) is dedicated to orange orchard cultivation. It is mainly irrigated by the flooding system, except for 3% to 4% of the surface (drip irrigation). The area is divided into 206 plots, belonging to 122 owners who constitute a community of irrigators. The slope in the study area is less than 4%.

Currently, irrigation water is sourced directly from the Guadalquivir River, which is then elevated to the main irrigation canal through pumping. The pumping station consists of two motors, each with its
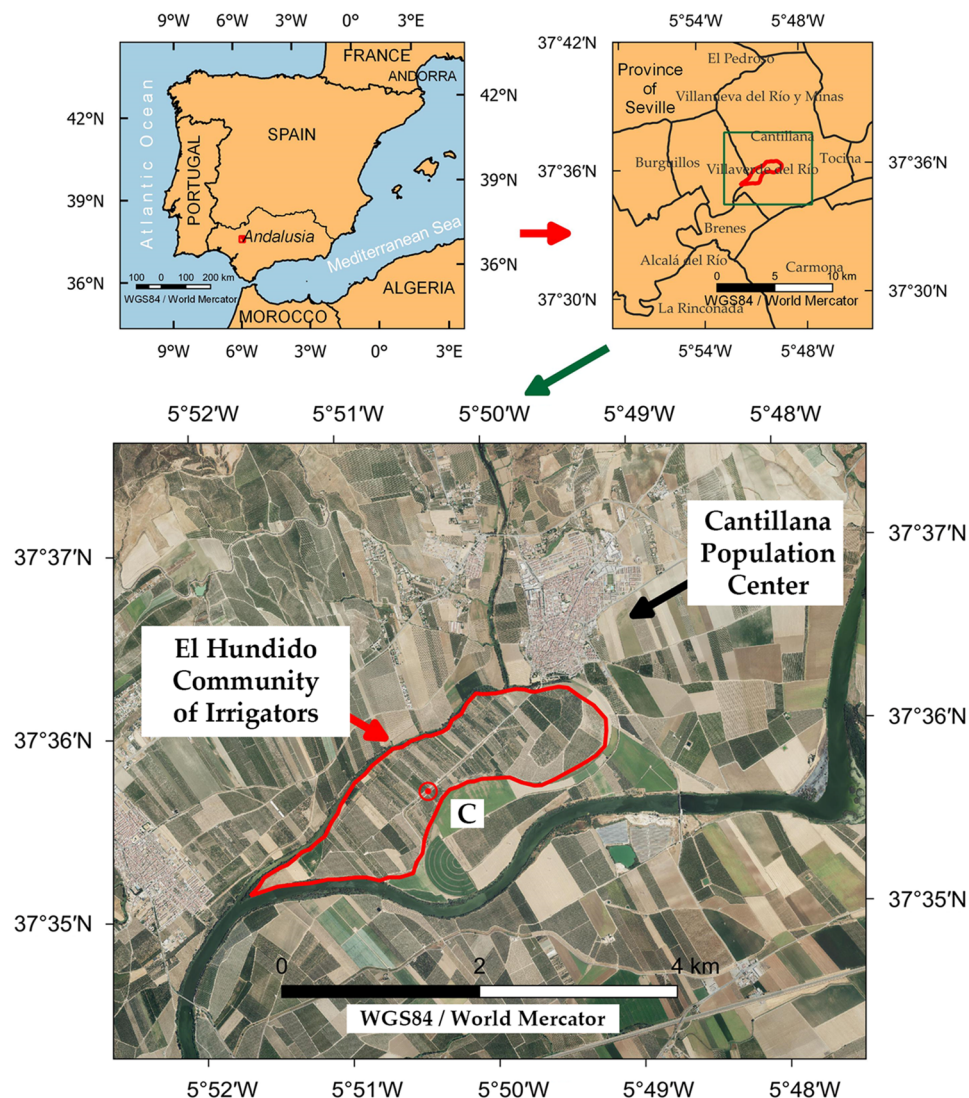

Figure 1. Location of the study area and arrangement of its crops.

respective pump, and steel pipes. To enable gravity irrigation of the entire study area, a concrete channel was built (into which the pumped flow of the Guadalquivir is poured).

All plots are distributed along both banks of the canal and receive water from a series of intakes arranged along the entire pipeline, configuring a network of thorn-form ditches. Additionally, the irrigated area has four wells located next to the canal and in the middle of its route that, if necessary, can pump water to the main canal. The total flow rate of these wells amounts to 120 l/s.

Finally, it is worth noting that this research's study area is highly representative of its significant role in both national and international citrus trade.

2.2. Citrus orchards characteristics

The study area's citrus plantations, with a mean age of 15 years, were grown with an average spacing of 5 m between rows and 3.5 m between trees within the row.

To have production throughout most of the year, the El Hundido community of irrigators has a wide variety of cultivars (Navelate, Navelina, Lane Late, Salustiana, and Chislett) grafted onto the Carrizo citrange rootstock (Hayat et al., 2022). They all originate from spontaneous or induced mutations of established orange varieties, are characterized by vigorous trees, notable organoleptic qualities, and fruit well-suited for fresh consumption or juice production, each with distinctive features in flavor, color, and ripening time (Seminara et al., 2023; Singh et al., 2021).

2.3. Climatology and physical environment

Water is the main limiting factor for the productivity and profitability of citrus plantations in Cantillana. Climate data retrieved from Copernicus Climate Change Service information between 1991 and 2021 (Climate Data, 2024) reveal that Cantillana's characteristic precipitation pattern is seasonal (with a marked summer drought) and insufficient (521 mm of annual rainfall compared to the approximately 1,200 mm needed annually by a mature plantation). Therefore, irrigation is one of the most important cultivation practices for achieving optimal fruit production and quality.

However, Cantillana not only faces issues of water scarcity and/or low quality in many of its citrus-producing areas, but climate change also threatens to worsen this situation by the end of the 21st century (Pérez-Pérez et al., 2020). This will further reduce available irrigation water and prolong droughts, intensifying aquifer exploitation and degrading water quality.

In addition to the effects of climate change on the availability and quality of water for irrigation, other effects on environmental conditions are expected, such as increased temperatures (average annual temperature of 18.8 °C in Cantillana (Climate Data, 2024) and other adverse climatic phenomena, as well as impacts on soil quality (erosion, loss of organic carbon, and decreased biodiversity). These factors could affect the physiology of the trees, threatening the development, production, and profitability of the crops.

For this research work, concerning the climate evolution of the study area, precipitation and temperature variables have been considered, respectively, from 2006 to 2100 (Ministerio para la Transición Ecológica y el Reto Demográfico, 2024). As a starting point, the average values of these variables were considered under the SSP3–7.0 Scenario and the MCG CMCC-ESM2 mathematical model from the Local Climate Change Scenarios of the Junta de Andalucía (Andalusian Regional Government), based on the 6th report of the Intergovernmental Panel on Climate Change () for the Consejería de Sostenibilidad' Medio Ambiente y Economía Azul (Junta de Andalucía) (IPCC, 2022).

Regarding the physical environment, and according to Fernández Cacho et al. (2010), the municipality of Cantillana is divided into two distinct areas. The first includes the urban center and the entire South from the Arroyo Valsequillo, Ricache and Carretera de Córdoba. The rivers, in their descent from the mountain range, have carried clays (alluvial deposits), to form a plain known as the Vega del Guadalquivir. The second area corresponds to the north of the municipality and features a more varied orography, characterized by alternating plains and mountains. Its average altitude varies from 50 to 150 m, rising in the western vertex where the highest heights are reached, with Loma de Enmedio at 316 m the highest peak. These lands, formed from various types of rocks, are resistant to erosion: slate and agglomerates in the lower areas, and dark granites and basalts at the highest elevations in the North.

2.4. Data and preprocessing

2.4.1. Fieldworks

Field data collection was carried out within a five-year research project from 2015 to 2020 (the first project indicated in the Funding section) to infer, among other parameters used in this paper, the Citrus orchards LAI located in the study area. Specifically, the LAI measurement was carried out using a representative sample of ten specimens (from each one, 50 leaves were chosen, evenly distributed throughout the tree crown) per citrus plot. The length and width of each leaf were then measured to obtain the unit area per leaf (oval shape). Afterwards, all the values for each leaf per tree were added up, and finally, the results per tree were averaged (see Eq. (1)).

$$LAI = \frac{Leaf\,area \cdot Tree\,density\,per\,plot}{Plot\,area} \tag{1}$$

On the other hand, in September 2020, fieldwork was carried out in all the citrus orchards of the El Hundido community of Irrigators in Cantillana to establish field control points (the second research project mentioned in the Funding section). The process of mapping was carried out utilizing a portable GPS device to identify three separate management units that had diverse agricultural backgrounds. These histories provide information about the land kind or use before the establishment of citrus orchards, the moment of conversion into citrus orchards, and the cropping patterns used for each year of land use as citrus orchards. The city council of Cantillana supplied the documents of these histories. Furthermore, data were collected in every citrus plot within the El Hundido community of Irrigators.

2.4.2. Sentinel-1 time series data

According to the ESA (2024a, 2024b, 2024c), the Sentinel-1 mission captures images using C-band SAR technology regardless of weather conditions, both during the day and at night. Sentinel-1A was deployed on 3 April 2014, whereas Sentinel-1B was deployed on 25 April 2016. Sentinel-1A incorporates SAR imaging in four distinct imaging modes, each offering varying resolutions (as low as 5 m) and coverages (up to 400 km). This mission captures data using both horizontal and vertical polarization, has extremely short intervals between revisits, and delivers products quickly. One Sentinel-1 satellite can potentially create a map of the whole landmasses on Earth using interferometric wide (IW) swath mode every 12 days in a single pass, whether it is ascending or descending. The two satellites provide a precise repeat cycle of 6 days at the Equator. Due to the variation in orbit track spacing with latitude, the revisit rate is considerably larger at higher latitudes compared to the Equator.

In this work, 294 Sentinel-1A images were downloaded from the Copernicus Browser under the Copernicus Data Space Ecosystem (ESA, 2024c). The image date frame was from 1 January 2021 to 31 December 2022 (from now on, full time range). All satellite images were downloaded as 8-bit TIFF 'enhanced visualization', sized 2500x1380 pixels, and with a resolution of 72 dpi (Figure 2).

Sentinel-1A C-band SAR images were provided in IW mode, utilizing a dual polarization method (VV + VH). The photos were disseminated as Level-1 products, specifically as single look complex (SLC) and ground range detected (GRD) on all dates. The ground resolution for SLC imagery is 5 m × 20 m, whereas for GRD images it is 10 m. The acquisition of all the images was done in ascending mode, with incidence angles varying between 38.87° and 39.26°. Sentinel-1A Level-1 SLC and GRD assets used were in high resolution. According to the ESA (2024b), for the Sentinel-1 IW products, multi-looking is performed on each burst individually. All bursts in all sub-swaths are then seamlessly merged to form a single, contiguous, ground range detected image per polarization. However, since the usual SAR data processing, which generates Level-1 images, does not incorporate radiometric corrections, and there is still a considerable radiometric bias, it becomes imperative to apply radiometric adjustments to the SAR images. Further, the radiometric correction is necessary when comparing SAR images obtained from the same sensor but at various time points, as demonstrated in this study. The process of radiometric calibration was implemented by utilizing Eq. (2) as described by MacDonald' Dettwiler and Associates Ltd (MDA 2011).

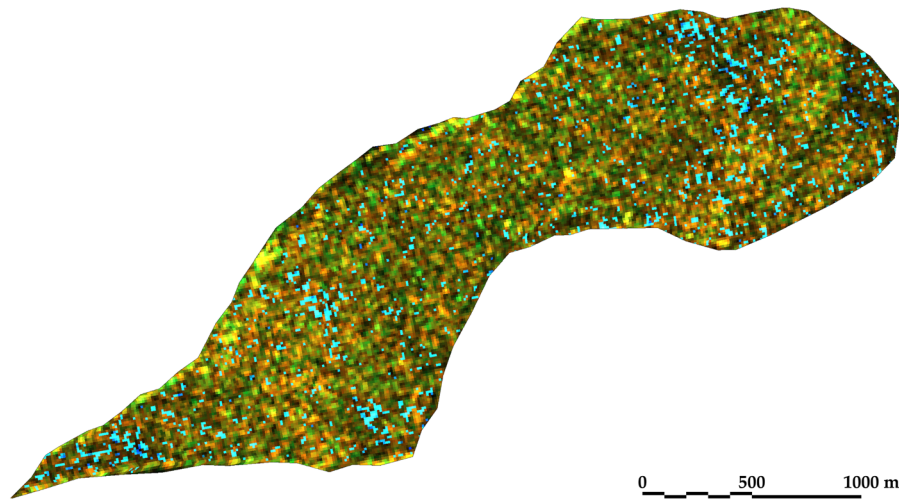$$\gamma_i = \frac{\left(DN_i^2 + b\right)}{A_i} \tag{2}$$

Figure 2. Sentinel-1 IW (VV+VH) Enhanced visualization image. Case study area with scale. Coordinates of the study area centroid are 37.59458° N 5.84059°W, and those for the southwesternmost point (bottom-left corner) are 37.585497° N, 5.861256° W.

In Eq. (2), the gamma calibration vector for the i-th element is denoted as A_i, the constant offset is represented by b, and the intensity is indicated by DN_i^2. Level-1 products include four calibration look-up tables (LUTs) that can be used to generate $\beta_i^0, \sigma_i^0, \gamma_i$, or a digital number (DN). The Look-Up Tables (LUTs) implement a gain that varies with the range, incorporating the absolute calibration constant. Regardless of the chosen LUT (in this case, σ_i^0), for each pixel 'i' that lies between points in the LUT, the Ai value is determined by bilinear interpolation.

Despite the above, the enhanced visualization Copernicus script-product (ESA, 2024c) used in this work combines the already calibrated gamma of the VV and VH polarizations in a false color visualization. This script-product shows all pixels with surface water in cyan, while land appears in different shades of yellow/green. Vegetated areas are shown in mustard green and bare ground in a darker green. Each month, Copernicus enhanced the visualization script-product to offer between 7 and 11 images.

According to the ESA (2024b), Sentinel-1's Enhanced Visualization imagery includes cyan points that often highlight features or phenomena identified during processing. These colors do not represent natural tones but emphasize elements significant in radar data.

- Sentinel-1 and radar imagery: Sentinel-1 uses SAR, emitting radar signals and capturing their reflections. As the imagery is not based on visible light, it requires Enhanced Visualization methods to improve interpretability.
- Calibrated data: Calibrated and radiometrically corrected radar signals accurately reflect surface characteristics, e.g., roughness, moisture, and structure. Calibration ensures consistent backscatter intensity.
- Meaning of cyan points:
- Cyan in Enhanced Visualizations: Cyan, which blends blue and green, is frequently utilized to highlight specific artificial objects, cities, or intense reflections. In SAR images, these predominantly represent regions with significant radar reflectance, including structures like buildings, bridges, or other metallic constructs that effectively bounce back the radar signal.
- Cyan points in unexpected locations may suggest a particular type of land cover, geological feature, or even regions with standing water or ice, e.g., smooth surfaces such as tranquil water bodies or flat roofs can occasionally reflect radar in a manner that produces cyan shades in enhanced products.
- Other Possible Meanings:
- Based on the context, the cyan points may indicate areas of significant radar backscatter change between two observations.
- Cyan points may sometimes indicate regions of limited or sparse vegetation based on the interaction between the radar signal and the terrain.

2.5. Methods

The methodological approach is depicted in Figure 3 and developed in the following subsections.

2.5.1. Evolutionary algorithms

This section provides an overview of genetic algorithms, an optimization technique inspired by the principles of natural selection. This foundational knowledge supports the development of the new CARP flux model, which aims to estimate water requirements for citrus orchards.

Biological processes drive the evolution of living organisms (Gupta, 2020). Genetic algorithms mimic natural selection by assigning individuals a fitness score that reflects their adaptive, competitive, and reproductive capabilities within a model. Those with higher fitness have a greater chance of contributing to subsequent generations, thereby increasing the success of certain genetic lineages (Gupta, 2020).

The efficacy of a genetic algorithm depends on its programming quality. These algorithms address problems without established solutions (Ramírez-Juidías et al., 2015) and improve outcomes when only partial solutions exist.

A genetic algorithm comprises five distinct phases: initialization of an initial population, evaluation of a fitness function, selection of individuals, crossover of genetic material, and mutation of selected individuals. The population embodies the challenges to be addressed. The individual is distinguished by the A1 and A2 binary data (gene and chromosome). The fitness function quantifies the binary code's capacity to solve the problem. The selection comprises the programming that will ascertain the optimal combinations of 'genes' and 'chromosomes' to be read, hence determining the most effective programming code for solving the given task. The crossover phase is the most pivotal stage in the genetic algorithm. The crossover point is selected at random and reflects the genetic material from each 'parent' that is utilized to solve the problem.

Similar to offspring in biological organisms, genetic algorithms can yield random mutations. Although mutations may initially seem detrimental to a population, they prevent premature convergence; i.e. in an algorithm, this is when a satisfactory solution has been reached.

Understanding evolutionary algorithms involves the following steps:

- Objective function definition → The evolutionary algorithm is applied to minimize the error in the estimation of ET_c as per Eq. (4). The optimization objective is to determine the best-fitting functions for K_c, K_{cb}, and ET_0, using LAI and other remote sensing-derived parameters. The error function to minimize is the difference between the modeled and observed ET_c over a known time series.

$$LAI = \frac{Leaf\ area \cdot Tree\ density\ per\ plot}{Plot\ area} \qquad LAI = 0.2273 \cdot e^{(4.9721 \cdot GNDVI)}$$

$$LAI(VV) = 0.075 \cdot \gamma_{VV}(dB) + 3.41$$

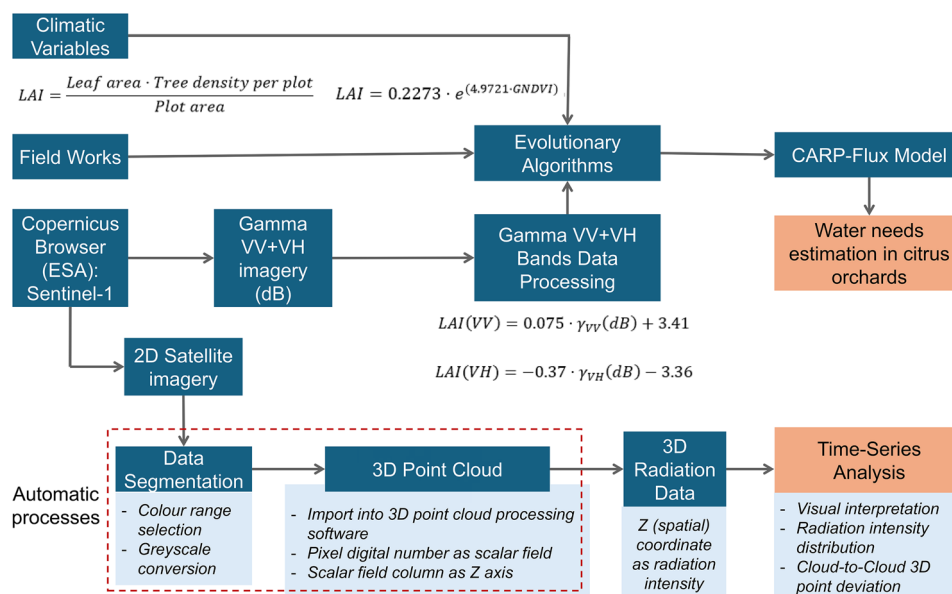$$LAI(VH) = -0.37 \cdot \gamma_{VH}(dB) - 3.36$$

Figure 3. Methodology flowchart carried out in the study area.

- Solution encoding and representation → Candidate solutions (chromosomes) are encoded using real-valued representations corresponding to coefficients in empirical relationships. For example, in Eq. (11), all constants were optimized through the genetic algorithm by encoding them as gene values within the chromosome. A similar process was carried out for Eqs. (12) and (13).
- Fitness function → The fitness function evaluates how well each solution estimates ET_c and water demand using radar-derived LAI inputs. A higher fitness score corresponds to lower root mean square error (RMSE) between observed and modeled water needs at the plot level.
- Optimization of model equations → Using this process, the evolutionary algorithm optimized: a) The empirical function relating GNDVI to LAI [Eq. (13)]; b) The functions relating LAI to K_c and K_{cb} [Eqs. (11) and (12)]; c) The equation for ET_0 as a function of LAI and the monthly adjustment factor f [Eq. (10)]; d) And indirectly, the estimation of K_s via temperature ratios [Eq. (6)], and K_e [Eq. (9)] from the rest of the components.
- Parameter refinement and generalization → The final equations used in the CARP-flux model were those yielding the best performance across the Sentinel-1 time series data from 2021–2022. The genetic algorithm was instrumental in fitting these equations to local environmental conditions in the Guadalquivir Valley, ensuring the parameters are both accurate and robust.

The application of a genetic algorithm was crucial to developing the new model flux, which infers water requirements in the study area through the patented process by E. Ramírez-Juidías et al. (2015).

2.5.2. Data processing
According to Navarro et al. (2016), the gamma VV+VH bands were utilized to ascertain the average value for each plot of citrus orchards and for each time period. After computing the average values, they were transformed from a power scale to a logarithmic scale to accurately represent decibel (dB) values using Eq. (3).

$$\gamma_i (dB) = 10 \cdot \log_{10} (\gamma_i), \tag{3}$$

where γ_i represents the gamma-calibrated backscattering coefficient that has been obtained from Eq. (2) for each pixel of the SAR images.

2.5.3. Modeling the water requirements for citrus orchards in the study area
As is well known, crop irrigation requirements refer to the total amount of water, measured in millimeters, that is applied to the crop during the entire irrigation season in order to fully meet the crop's water needs (Doorenbos & Pruitt, 1977; Food & Agriculture Organization of the United Nations (FAO), 2024).

According to the FAO (2024), Doorenbos and Pruitt (1977), Steduto et al. (2012), and Tenreiro et al. (2021), the general model to obtain ET_c is the one shown below (Eq. (4)):

$$ET_c = K_c \cdot ET_0 = (K_s \cdot K_{cb} + K_e) \cdot ET_0 \tag{4}$$

Eq. (4) represents the relationship between several factors in the ET_c (mm/day) calculation. K_{cb} is the basal crop coefficient, K_e is the soil evaporation coefficient, K_s is the water stress coefficient, and ET_0 (mm/day) represents the reference crop evapotranspiration. K_s elucidates the impact of water stress on agricultural transpiration. In situations when soil water is a limiting factor, the value of K_s is less than 1. Conversely, when there is no stress on the soil water, the value of K_s is equal to 1. K_c is the crop coefficient.

Conversely, the amount of atmospheric water vapor in the study area is crucial, as it directly affects optical depth and thus the intensity of reflected radiation per pixel.

Similarly, according to Ramírez-Juidías and José Cabello-Franco (2023), direct solar radiation lacks sufficient heat to warm the atmosphere; instead, the soil converts part of the incident radiation into Short Wave Infrared (SWIR) radiation, which effectively heats the lower atmosphere. Physically, the temperature rise increases molecular speed and the frequency of collisions. If the SWIR-induced heating persists

alongside rising water vapor near the plant canopy, molecular speeds reach a level where high-speed elastic collisions cause the wave fronts to couple, forming a plane wave front. This leads to a phenomenon known as thermal plugging, resulting in a decrease in Photosynthetically Active Radiation (fAPAR) (Ramírez-Juidías, 2022). Eq. (5) shows the relationship between fAPAR and average environmental temperature (AET), in Celsius, affecting the plant canopy (Ramírez-Juidías, 2022):

$$fAPAR = 0.564 - 0.011 \cdot AET \left(r = 0.83;\ R^2 = 0.7;\ p \leq 0.001 \right) \tag{5}$$

At this point, the air layers progressively warm toward the canopy surface, leading to a decrease in relative humidity (RH, %). This temperature-dependent change significantly impacts the plant's water stress and, therefore, K_s. In short, the resulting thermal inversion leads to a stress increase within the soil-plant-atmosphere system.

For this reason, Eq. (6) shows a new form of the water stress coefficient:

$$K_s = \frac{T_{mean}}{T_{max}} \left(r = 0.901;\ R^2 = 0.89;\ p \leq 0.001 \right) \tag{6}$$

where T_{mean} is the mean temperature and T_{max} is the maximum temperature, both in Celsius, of the minimum period considered for data collection in the study. In this work, the temperature and precipitation data are daily and have been downloaded from the Crop Monitoring application (EOS Data Analytics, 2024).

Meanwhile, according to Ramírez-Juidias et al. (2024), the use of the G band in the GNDVI is associated with the fAPAR and is directly linked to the LAI. Therefore, GNDVI has a higher level of sensitivity toward chlorophyll content compared to NDVI. For this reason, regarding the calculation of both the K_c and the K_{cb} (Allen & Pereira, 2009; Pereira et al., 2020), and using evolutionary algorithms, the following equations (Eqs. (7) and (8)) were obtained based on the LAI, each of which was used in the present work. Under a user license, the Crop Monitoring application was used to download data corresponding to the GNDVI at different temporal resolutions, ranging from one to three days, utilizing both the PlanetScope satellite constellation and the Sentinel-2 L2A. The application automatically resizes the value per pixel based on the series of satellite images from which the user wishes to obtain said value, being GNDVI in this case study. These equations will be developed in the Results section.

$$K_c = f(LAI) \tag{7}$$

$$K_{cb} = f(LAI) \tag{8}$$

Thus, and considering Eqs. (4), (9) determines the soil evaporation coefficient (K_e):

$$K_e = K_c - K_s \cdot K_{cb} \tag{9}$$

Finally, the reference crop evapotranspiration (ET$_0$) (Eq. (10), after the adjustment obtained through evolutionary algorithms, also based on the LAI is:

$$ET_0 = \frac{LAI}{f} \tag{10}$$

where f is a factor dependent on the month considered (see Table 1).

Authors have called this new methodology CARP-flux.

2.5.4. From Sentinel-1 image data segmentation to 3D data modeling

In Antón and Amaro-Mellado (2021), Geographic Information System technology was used to compute the spatial Z coordinate from the digital number (DN) of each pixel in 2D infrared images, generating a 3D point cloud with 3D thermal data. However, since the source images were thermograms, they lacked

Table 1. Monthly factor f values for calculating ET_0 (mm/day).[a]

Jan	Feb	Mar	Apr	May	Jun	Jul	Aug	Sep	Oct	Nov	Dec
2.24	1.80	0.72	0.82	0.53	0.47	0.49	0.54	0.98	1.20	2.19	3.43

[a]Values obtained through evolutionary algorithms for citrus orchards from the Vega del Guadalquivir. 'f' is a function of the average daily precipitation (P) of each month existing in the study area for a statistically significant period of at least 30 years (Climate Data, 2024). It can be obtained through the following relationship $f = 0.5 + 0.95 \cdot P$ (r = 0.79; R^2 = 0.73; $p \leq 0.01$).

Figure 4. Automatic data segmentation. Satellite image conversion into grayscale.

differentiation between color shades and contextual details, requiring full-pixel processing for scene characterization. This DN-based method has also been used to compute 3D point cloud intensities to detect surface damage (pathologies) in both modern and heritage buildings (Antón et al., 2022).

In contrast, this paper introduces a method that segments only the pixels containing relevant data from their context, generating a 3D point cloud containing 3D radiation data. This segmentation was performed automatically by selecting pixel color ranges using image processing software such as Adobe Photoshop, a technique already validated by the scientific community for vegetation analysis in desertified areas (Tong et al., 2024). Thus, in the present work, satellite data in the chosen enhanced-visualization TIFF image were within the intensity range of blue color, so pixels with such shades were discriminated. Although this segmentation process is considered accurate given the 0–255 levels in the 8-bit images used, which are determined by the satellite data themselves, these selected data were examined to determine if any possible pixels had been overlooked after the automatic color selection. Next, the image was converted into grayscale to ease the association of the study area's backscattering to each pixel's DN. The pixels that accounted for relevant data were thus distinguished against the uniform black background (Figure 4).

Following this image processing, the open-source CloudCompare (Girardeau-Montaut, 2016) software, widely used by the scientific community for point cloud processing, was utilized. It allows importing various image formats and exporting 3D ASCII point clouds in TXT, XYZ, PTS, or CSV. With an image resolution of 2500 x 1380 pixels, the resulting point cloud contained approximately 3.45 million points. Both the original image and the generated (flat, XY) point cloud represent each pixel's digital number (DN) as a Scalar Field, displayed by default using the 'blue-green-yellow-red' color scale. Before importing the ASCII file, the Scalar Field column was reassigned to the 'Z coordinate' attribute, automatically generating a third spatial dimension based on pixel grey tone intensity. The result is a monochrome point cloud (visualized in the 'Grey' color scheme), where Z values reflect backscattering data collected across the full time range (from 1 January 2021 to 31 December 2022) (Figure 5).

The dataset's intensity distribution is shown in 3D and can also be represented as a histogram of pixels across DN intervals to relate these data to the study area's water requirements. This will be explained in the Results section.

3. Results

3.1. Water requirements in the study area through the CARP-flux model

3.1.1. Estimation of crop and basal crop coefficients (K_c and K_{cb})

As previously specified (see Subsection 2.5.3), and taking into account Pereira et al. (2024), K_c and K_{cb} were obtained as a function of the LAI. This relationship is shown in Eqs. (11) and (12), respectively, below.

$$K_c = 0.2562 \cdot \ln(4.4 \cdot LAI) - 0.0902 \left(r = 0.964; R^2 = 0.929; p \leq 0.001 \right) \tag{11}$$

$$K_{cb} = 0.29 \cdot \ln(4.4 \cdot LAI) - 0.1 \left(r = 0.96; R^2 = 0.93; p \leq 0.001 \right) \tag{12}$$

As specified by Ramírez-Juidias et al. (2024), the GNDVI index is better suited for crops with dense canopies (mainly woody crops) or for more advanced growth stages in both woody deciduous crops and herbaceous crops. In contrast, NDVI is more appropriate for estimating crop vigor during early stages, particularly in herbaceous crops. This distinction is critical, not only because NDVI is more commonly used, but also because many studies, e.g. Tenreiro et al. (2021) and Bhatti et al. (2024), have reported limited results when using it. Moreover, NDVI-based models often rely on secondary variables with minimal influence on prediction outcomes (Martínez-Casasnovas & Bordes, 2005), especially for woody crops.

This work offers an innovative contribution by establishing the relationship between LAI and GNDVI specifically for citrus orchards in the Vega del Guadalquivir (Andalusia, Spain), based on over five years of field research (see Eq. (13)).

$$LAI = 0.2273 \cdot e^{(4.9721 \cdot GNDVI)} \left(r = 0.912; R^2 = 0.901; p \leq 0.001 \right) \tag{13}$$

3.1.2. Relationship between LAI and VV+VH backscattering time series

From Eq. (13), the full LAI time series for the study period was developed (Figure 6). LAI variations (2 to 4.5) reflect the citrus trees' phenological cycle, with growth in spring and early summer and reductions during dormancy or post-harvest. Seasonal irrigation, water stress in dry summers, Mediterranean climate factors, pruning, crop load, and microclimatic conditions also influence canopy density fluctuations.

Regarding VV and VH backscattering (Figures 7a and 7b), VV is generally higher on average than VH. VV ranges from −10.23 dB to −7.24 dB; VH ranges from −17.71 dB to −14.77 dB.
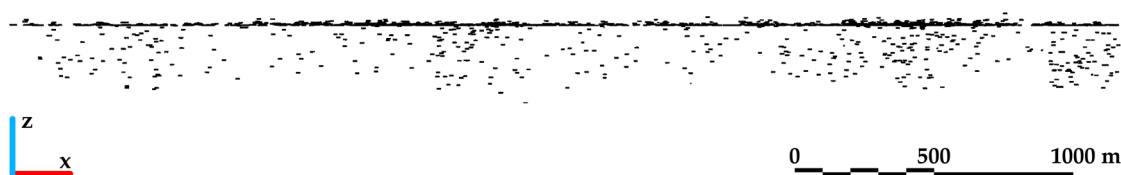

Figure 5. Spatial representation of the study area's backscattering. Full time range. Elevation view.
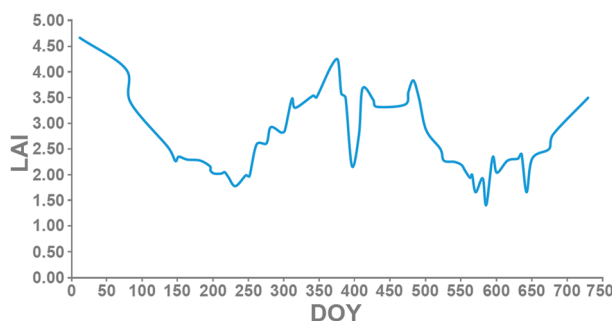

Figure 6. Mean LAI time series between 1 January 2021 and 31 December 2022.
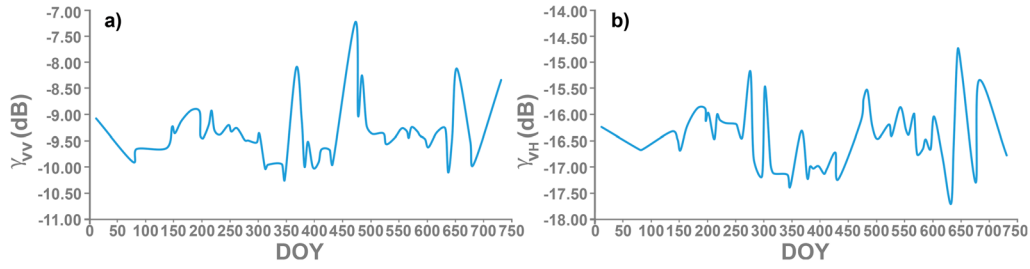
Figure 7. Mean backscattering VV (a) + VH (b) between 1 January 2021 and 31 December 2022.
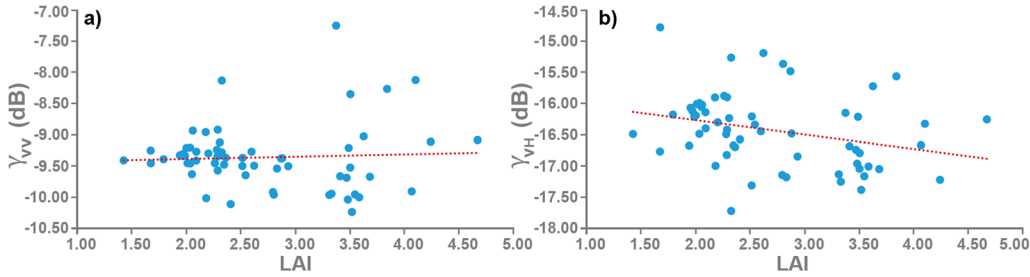

Figure 8. Comparison between mean backscattering values VV (a) + VH (b) and LAI from 1 January 2021 to 31 December 2022.

Comparing VV and VH backscattering with the LAI (Figures 8a and 8b) reveals a stronger linear relationship for VV (r = 0.29) than VH (r = 0.15), likely due to VH's weaker penetration. These correlation values suggest radar backscatter alone may not fully capture LAI complexity, so integrating other data sources like optical imagery or meteorological data can improve accuracy, as demonstrated in this study.

Based on the above, Eqs. (14) and (15) show the relationship between the LAI and the (VV+VH) backscattering.

$$LAI(VV) = 0.075 \cdot \gamma_{VV}(dB) + 3.41 \tag{14}$$

$$LAI(VH) = -0.37 \cdot \gamma_{VH}(dB) - 3.36 \tag{15}$$

From these equations, variables dependent on the LAI can be inferred to estimate the study area's water requirements from radar images. Despite moderate correlations, the LAI (Eqs. (14) and (15)) can be derived from radar backscatter to assess vegetation growth, optimize irrigation scheduling, and monitor ecosystem health in near real-time.

3.1.3. Comparison of K_c and K_{cb} time series

Figure 9 shows the crop coefficient (K_c) and the basal crop coefficient (K_{cb}) time series. They show a similar behavior, although the former generally has a higher value than the latter.

3.1.4. Comparison of K_s (water stress coefficient) and K_e (soil evaporation coefficient) time series

Figure 10 clearly shows that the coefficients K_s and K_e have an inverse relationship in practice. Likewise, the importance of the water stress coefficient (K_s) is evident.

3.1.5. Comparison between the reference crop evapotranspiration (ET_0) and gross irrigation needs (GIN) mean year

This work incorporates the concept of effective precipitation (P_e), in mm/month or mm/day (Eq. (16)), specified by Doorenbos and Pruitt (1977), to calculate gross irrigation needs (GIN). In the Guadalquivir
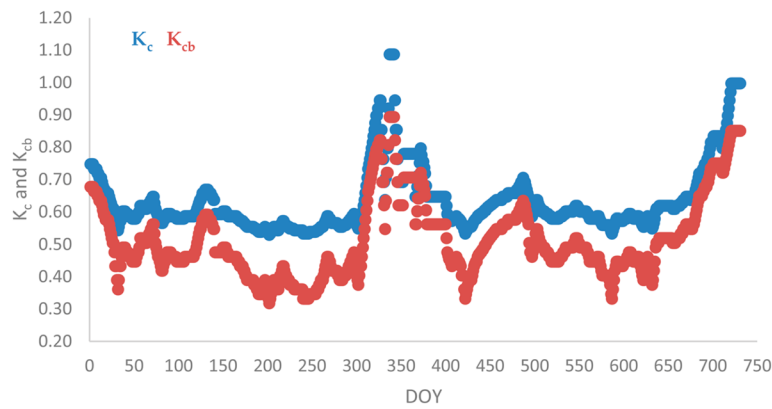
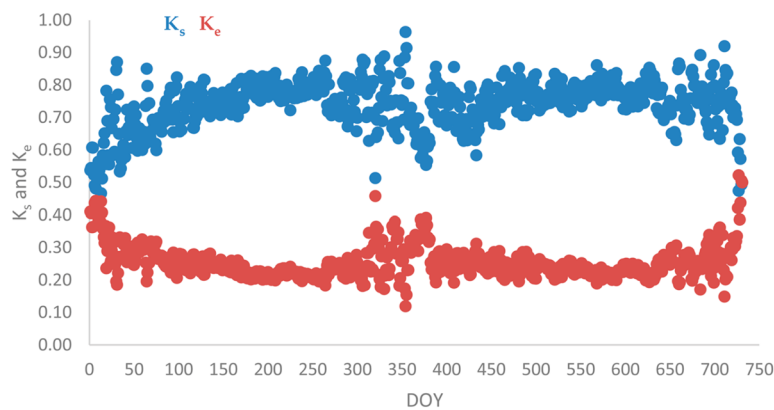**Figure 9.** Comparison between K_c and K_{cb} during the study period.

Figure 10. Comparison between K_s and K_e during the study period.

Valley, Pe is often computed daily using Eq. (16) due to the availability of daily precipitation data that meet its criteria. As noted in Subsection 2.5.3, the Crop Monitoring application (EOS Data Analytics, 2024) provided the daily precipitation (P).

$$P_e = 0.8 \cdot P - 25 \; if \; P > 75 \frac{mm}{month} \; or \; \frac{mm}{day}$$
$$P_e = 0.6 \cdot P - 10 \; if \; P < 75 \frac{mm}{month} \; or \; \frac{mm}{day}$$

(16)

where P = rainfall in mm/month or mm/day.

Based on this criterion, Eq. (17) can be used to infer the GIN in mm/day:

$$GIN \left(\frac{mm}{day} \right) = K_c \cdot ET_0 - P_e$$

(17)

Grounded on this, Figure 11 shows both the GIN and the ET_0 for the average year.

Comparing CARP-flux outputs with FAO56-based irrigation needs reveals that CARP-flux estimates higher water demand than the traditional Hargreaves method, better reflecting field conditions in the Vega del Guadalquivir, where soil moisture and humidity are generally high. Despite limited field irrigation records, model results were validated using available effective precipitation data and agronomic benchmarks, revealing consistent seasonal patterns.
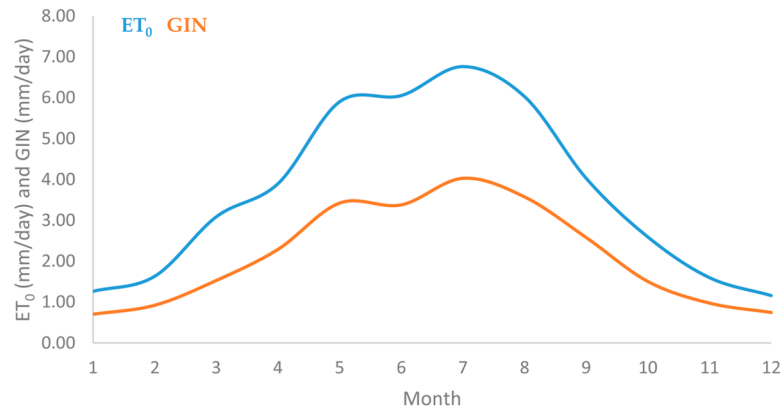
Figure 11. Values correspond to the mean year of the study period for gross irrigation needs (GIN) and reference crop evapotranspiration (ET_0).
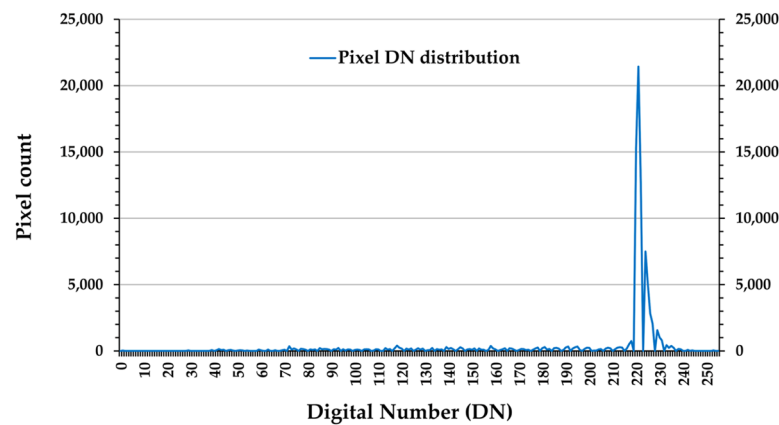

Figure 12. Intensity of satellite image pixels by their DN distribution. 1 January 21 to 31 December 2022.

3.2. Segmentation and spatial interpretation of sentinel-1 time series data

Figures 4 and 5 show the outcomes of the automatic processes developed from satellite images for data segmentation (Osco et al., 2023) and conversion into 3D point clouds. These processes allow for representing the intensity distribution of the datasets as a histogram of pixels across DN intervals. The distribution of the full-time range is depicted in Figure 12.

This histogram reveals that most of the pixels (70,177) deriving from the produced 3D radiation data fall within the 12 DN intervals ranging from 220 to 231, which represents 4.7% of the total DN range (0–255) and accounts for 76.22% of the total 92,071 pixels with radiation data. Consequently, the remaining 21,894 pixels (23.78% of the total) are spread among the rest of the intensity spectrum with an average value of 90 pixels (round up to the closest integer) per DN interval and a standard deviation of 108.13 pixels. Also, resulting from dividing the standard deviation by the mean, the coefficient of variation (CoV), with 1.21, is a clear indicator of the variability of the data.

From the above, further statistical data can be obtained to reveal the dispersion of radiation data and to quantify its global behavior in the case study area: a mean value of 359.65 pixels, with a standard deviation of 1902.91 pixels, and a CoV of 5.29.

Once the full time range was characterized, it is worth analyzing the best considered period of the year in terms of fruit quality: the last two weeks of August. In this way, the methodological processes described in this paper were applied to those instances in 2021 and 2022.

3.2.1. 15 to 31 August 2021
The satellite data downloaded from the Copernicus Browser is presented below (Figure 13).
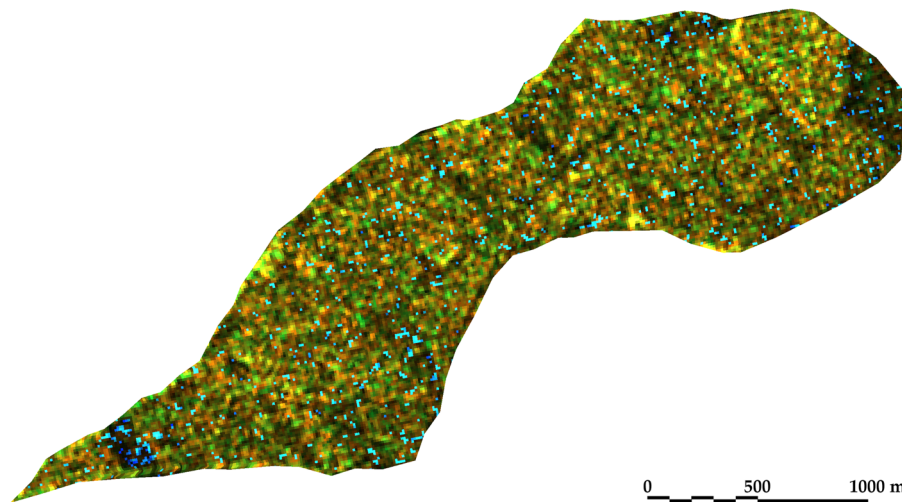
Figure 13. Sentinel-1 IW (VV+VH) Enhanced visualization image. Case study area with scale. 15 to 31 August 2021. Coordinates of the study area centroid are 37.59458° N 5.84059°W, and those for the southwesternmost point (bottom-left corner) are 37.585497° N, 5.861256° W.
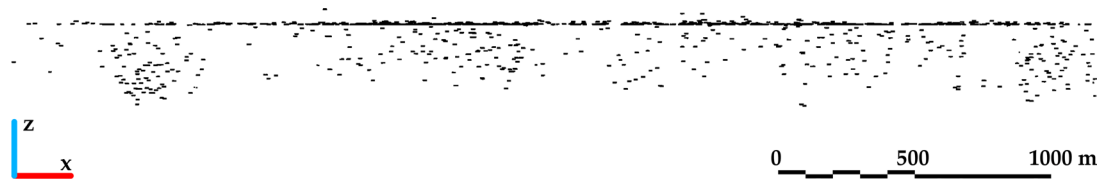

Figure 14. 3D radiation data of the case study area. 15 to 31 August 2021. Elevation view.
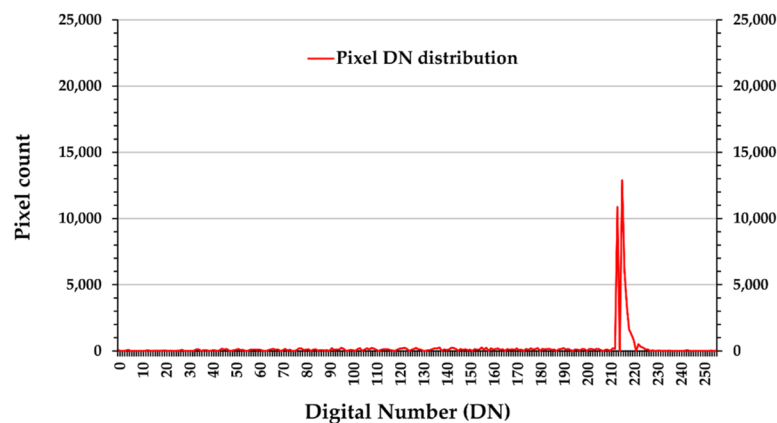

Figure 15. Intensity of satellite image pixels by their DN distribution. Mid-to-end of August 2021.

As seen above, the segmented radiation data was converted into a grayscale image to produce a flat point cloud whose third coordinate (Z) would be automatically determine using the image intensity (DN). Figure 14 shows the resulting 3D radiation data of the case study area for the specified time range, and Figure 15 presents the DN distribution. The scale of the graphs remains constant, with axes up to 25,000 pixels to ease comprehension.

As with the 2021–2022 data, most pixels (37,704) fall within 11 DN intervals from 213 to 223, which represents 4.29% of the total DN (0–255) and 66.91% of the 56,349 pixels with radiation data. For 15–31 August 2021, pixel intensities are generally lower compared to the full 2021–2022 period. The remaining 18,645 pixels (33.09%) are spread across the rest of the intensity range, averaging 76 pixels per DN interval (15.55% fewer than the full period) with a standard deviation of 70.23 pixels (35.05% lower). The CoV of 0.92 indicates reduced variability in this time frame.
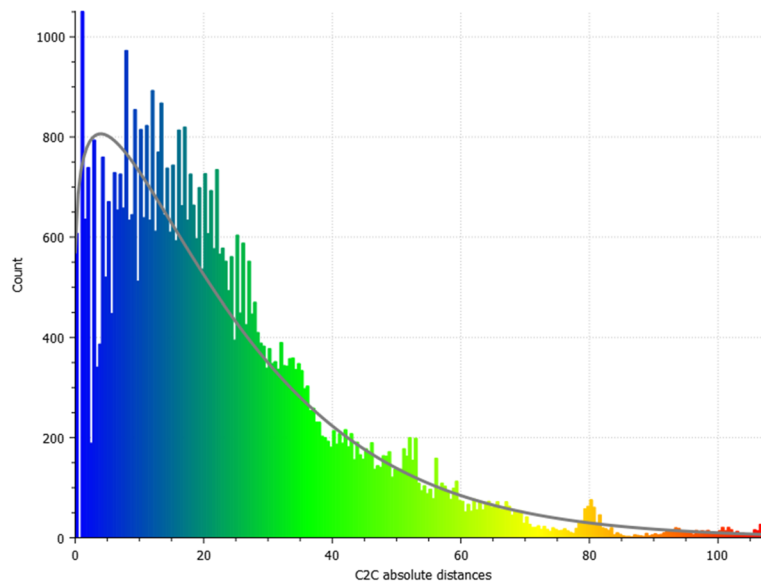
Figure 16. Radiation intensity comparison between 15 to 31 August 2021 and the full time range (2021–2022 period). Weibull distribution fitting curve.

The global DN distribution for the last two weeks of August 2021 shows a mean of 220.11 pixels, a standard deviation of 1133.35 pixels, and a CoV of 5.15, indicating less radiation data dispersion than the full 2021–2022 period.

To assess fruit quality, the difference between 3D radiation data from 15–31 August 2021 and the full 2021–2022 period was analyzed using CloudCompare, with the latter as the reference. The mean distance was 23.61 m, with a standard deviation of 18.33 m. Since the data were not normally distributed, a Weibull distribution provided a better fit (Figure 16). Distances in the Z coordinate represent radiation intensity, with meters serving as a spatial interpretation of this data.

The Weibull curve shows an asymmetric distribution, with its mode being 193.60 and a negative skewness near zero, in this case −0.23. The curve fitting was determined by the two Weibull parameters: $a = 4.84$ and $b = 203.07$. Its X^2 distance was 741,593, with a scalar field RMS error of 194.27 m. The distance of most points between clouds is below 40 meters.

The following period was also analyzed in terms of point cloud deviation to characterize a different instance of fruit production.

3.2.2. 15 to 31 August 2022

The satellite data downloaded from the Copernicus Browser is presented below (Figure 17).

Following this paper's methodology (from 2D enhanced visualization satellite imagery to 3D backscatter data), Figure 18 shows the 3D radiation data from 15 to 31 August 2022, and Figure 19 presents the DN distribution. The scale of the graph also remains constant.

The graph shows that most pixels (37,137) fall within 9 DN intervals from 194 to 203, representing 3.52% of the total DN range (0–255) and 59.01% of the 62,930 radiation data points. For 15 to 31 August 2022, pixel intensities are generally lower compared to the full 2021–2022 period and the same period in 2021. The remaining 25,793 pixels (40.99%) are spread across other intensity intervals, averaging 104 pixels per DN interval (15.55% higher than the full period and 36.84% higher than the previous year), with a standard deviation of 91.09 pixels, 15.76% lower than the full period but 29.70% higher than late August 2021. The coefficient of variation (0.88) indicates lower variability in this timeframe.

The global DN distribution of pixels in the last two weeks of August 2022 is characterized by 245.82 pixels in average, with a standard deviation of 1143.56 pixels and a CoV of 4.65. This selected time frame presents a lower dispersion of radiation data in comparison with the full 2021–2022 period. It is similar to August 2021 but with a higher average radiation, slightly higher standard deviation, and a lower coefficient of variation (a more constant behavior).
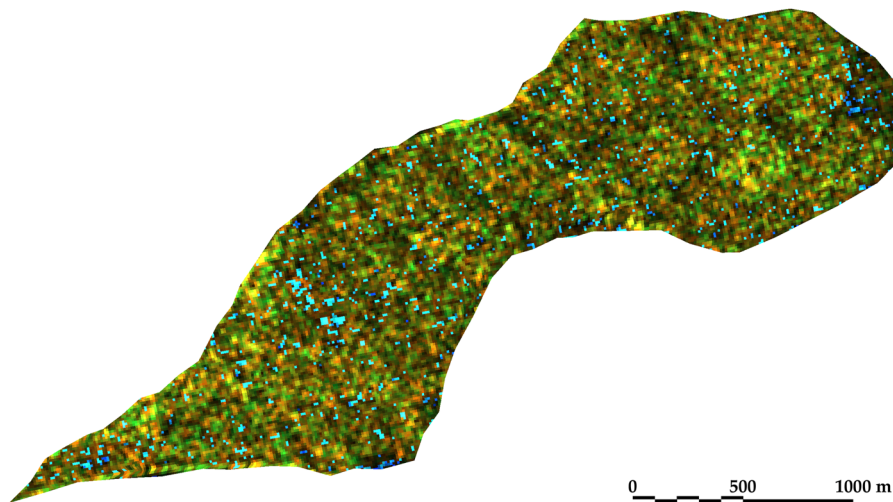
Figure 17. Sentinel-1 IW (VV+VH) Enhanced visualization image. Case study area with scale. 15 to 31 August 2022. Coordinates of the study area centroid are 37.59458° N 5.84059°W, and those for the southwesternmost point (bottom-left corner) are 37.585497° N, 5.861256° W.
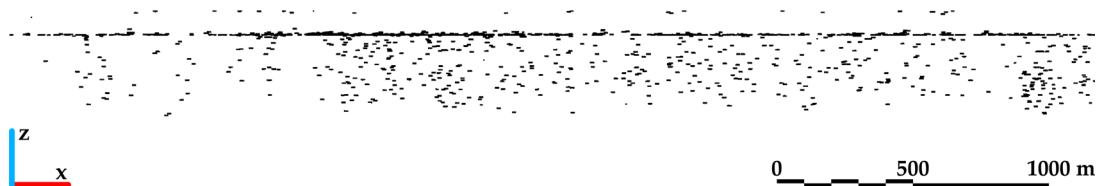

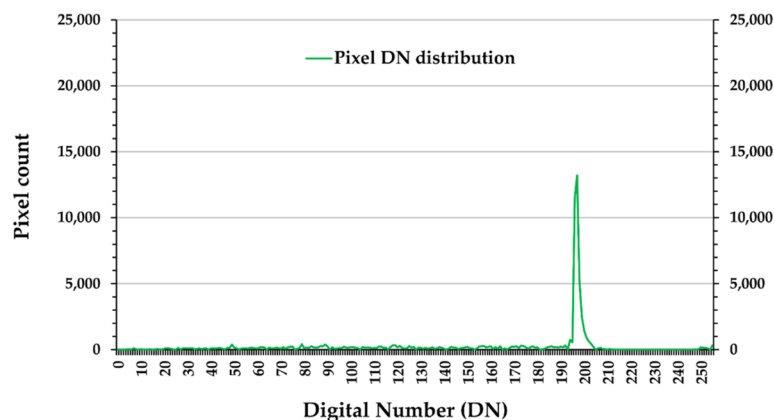**Figure 18.** 3D radiation data of the case study area. 15 to 31 August 2022. Elevation view.

Figure 19. Intensity of satellite image pixels by their DN distribution. Mid-to-end of August 2022.

Finally, the difference in 3D radiation data between the selected period (15 to 31 August 2022) and the full-time range (reference) was also studied through point deviation analysis with Weibull distribution fitting (Figure 20). Units: points and meters.

The Weibull curve shows a smoother distribution against the comparison between August 2021 and the full time range (from 2021 to 2022), with its mode being 0 and a positive skewness of 2.02. The curve fitting was determined by the two Weibull parameters: a=0.99 and b=24.95. Its X^2 distance was 5702.42, with a scalar field RMS error of 33.45 m, significantly lower than that when comparing the previous year with the full time range. The distances of most points between clouds are below 30–40 meters, which should imply a greater similarity to the whole period in relation to the August 2021–full time range analysis.
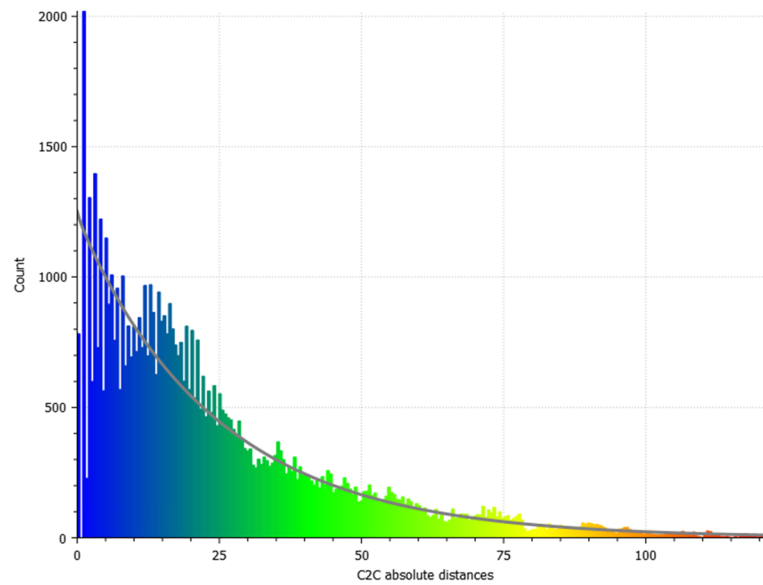
Figure 20. Radiation intensity comparison between 15 to 31 August 2022 and the full time range (2021–2022 period). Weibull distribution fitting curve.
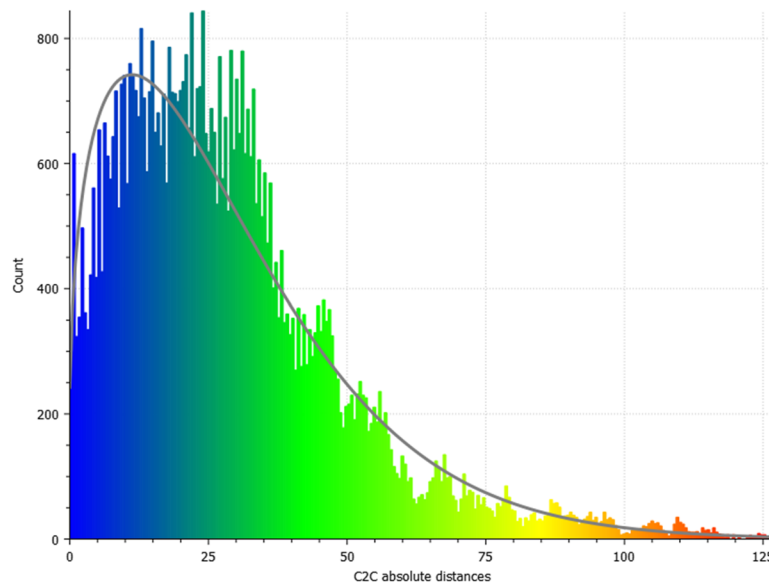

Figure 21. Radiation intensity comparison between 15 to 31 August 2021 and 15 to 31 August 2022. Weibull distribution fitting curve.

3.2.3. 15 to 31 August 2021 against 15 to 31 August 2022

Finally, the last two weeks of August 2021 and those of the same month in 2022 were also analyzed to show how the study area radiation evolved in one year. This was carried out through C2C (Cloud-to-Cloud) point deviation analysis in CloudCompare software, with the first period as the reference in the comparison (Figure 21). This yielded a mean distance of 29.14 m and a standard deviation of 20.82 m.

The Weibull curve exhibits an asymmetrical distribution, with a mode of 11.45 and a positive skewness of 1.28. The curve fitting was determined by the two Weibull parameters: $a = 1.34$ and $b = 24.95$. Its X^2 distance was 3362.64, with a scalar field RMS error of 35.81 m. The distances of most points between clouds are below 40–60 meters, which, in turn, implies a greater similarity to the whole period in relation to the August 2021–full time range analysis.

To display these findings together, Figures 22 and 23 present the DN distributions and point cloud distances, respectively, with Weibull curve fitting of the different periods analyzed.
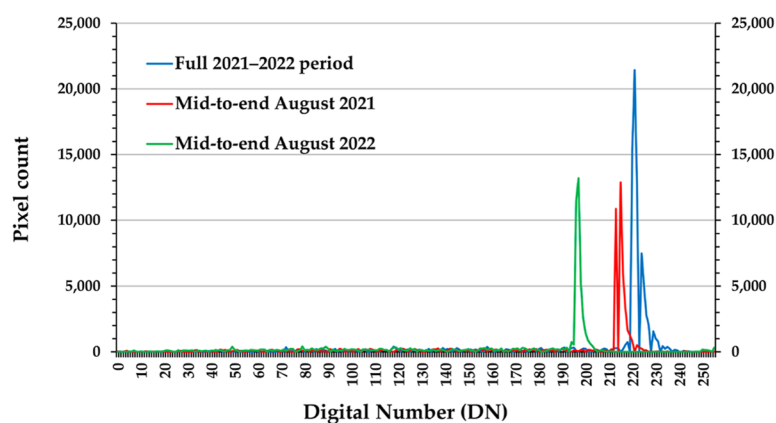
Figure 22. Intensities of satellite image pixels by their DN distribution: blue) 1 January 2021 to 31 December 2022; red) Mid-to-end of August 2021; and green) Mid-to-end of August 2022.
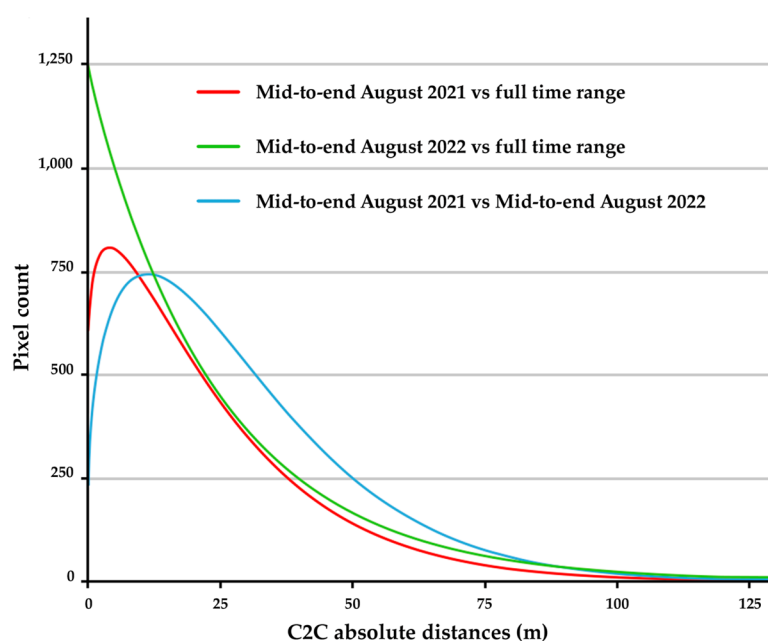

Figure 23. Weibull distribution: red) Last fortnight of August 2021 vs full time range; green) Last fortnight of August 2022 vs full time range; and blue) Last fortnight of August 2021 vs that of 2022.

Table 2. Statistical data of radiation data Weibull distribution across different periods, where Sd is the standard deviation, and CoV represents the coefficient of variation.

a) 15 to 31 August 2021		b) 15 to 31 August 2022		Comparing a) and b)	
Statistical descriptor	Value	Statistical descriptor	Value	Statistical descriptor	Value
Mean (points)	236.76	Mean (points)	250.72	Mean (points)	250.72
Sd (points)	267.07	Sd (points)	316.45	Sd (points)	269.20
CoV	1.13	CoV	1.26	CoV	1.07
Mean up to 40 m (points)	536.22	Mean up to 40 m (points)	611.04	Mean up to 40 m (points)	487.50
Sd (points)	208.99	Sd (points)	322.82	Sd (points)	212.14
CoV	0.39	CoV	0.53	CoV	0.44
Mean from 40 m (points)	61.08	Mean from 40 m (points)	75.89	Mean from 40 m (points)	37.25
Sd (points)	62.57	Sd (points)	68.23	Sd (points)	30.32
CoV	1.02	CoV	0.90	CoV	0.81

The Weibull distributions of points in the comparison between the different periods are statistically characterized in Table 2.

Both the histogram and data show many points clustered near zero distance, indicating that most areas experienced minimal (but measurable) changes in dryness between the analyzed dates. However,

several sectors (pixels) showed notable changes in radiation intensity. Variability for distances beyond 40 meters is about three times higher than for shorter distances, though these points are fewer and less dispersed.

Results show a clear left-skewed distribution of point deviations between 15–31 August 2022 and the full time range, indicating fewer changes overall. Still, a significant number of drier areas at greater distances exhibit higher variability, though closer areas are more numerous. Overall, mid-to-late August 2022 displays greater dispersion and a higher average point count per distance interval compared to the same period in 2021.

Both qualitatively and quantitatively, the histograms and statistics show greater variability and longer tails in point distances between August 2021 and August 2022 than in the full 2021–2022 period, indicating significant changes in the study area over one year.

4. Discussion

Radar remote sensing offers numerous uses, including sustainable forest management, crop condition monitoring, soil property analysis, and accurate mapping of tillage activities, among others (ESA, European Space Agency (ESA),), 2024a). Interferometric SAR detects surface movements with millimeter-level precision annually, making it a reliable tool for monitoring land subsidence, structural damage, and underground construction, thus improving safety and reducing economic loss.

According to the ESA (2024b), Sentinel-1 images monitor changes in agricultural production and pasture productivity due to drought, as well as land degradation from over-cultivation, grazing, and poor irrigation. Agricultural maps provide unbiased assessments of cultivation levels by country or season, aiding food security efforts in vulnerable regions.

Sentinel-1 was chosen for this study due to its free, unrestricted access, all-weather, day-night C-band SAR imaging, and frequent 6-day revisit interval, ideal for monitoring dynamic environments. Compared to TerraSAR-X, Sentinel-1 offers a wider swath (250 km vs. 30 km), shorter revisit time (6 vs. 11 days), and free data, making it better suited for large-scale, time-sensitive applications. It also outperforms ALOS with a faster revisit (6 vs. 14–46 days), wider coverage, and better global reach. While ALOS's L-band excels in forest and biomass monitoring, Sentinel-1's C-band delivers higher spatial resolution for most land-use and environmental uses, making it more versatile for diverse Earth observation needs.

Meanwhile, and building upon prior research (Dela Torre et al., 2021; Zhao et al., 2024), the present study has verified that the temporal fluctuations of backscattering coefficients may accurately represent the changes in the development of citrus orchards.

Figure 6 shows that sharp drops in LAI correspond to harvesting periods (days 30, 243, 350, 575, 608, 650, and 700). This pattern is also seen in the crop coefficient (K_c) and basal crop coefficient (K_{cb}) in Figure 9, confirming the link between LAI, K_c, and K_{cb}.

Although the (VV+VH) backscatter time series (Figure 7) follows a similar trend, it cannot distinguish between harvesting periods and phenological development in citrus orchards. This suggests the temporal baseline used maintains strong coherence despite changes from climate, farming practices, or crop growth. Also, this study found a strong correlation between coherence fluctuations and backscatter changes linked to orchard development, highlighting the importance of combining Sentinel-1 imagery with field studies for accurate differentiation.

The correlation between LAI and backscatter (VV+VH) is stronger with gamma VV backscatter (r = 0.29), consistent throughout the entire study period and at its start and end (see Figure 8). As Navarro et al. (2016) specified, this may clarifies why the correlation between gamma VH backscatter and LAI (r = 0.15) is notably lower over the entire period.

When examining K_s (water stress coefficient) and K_e (soil evaporation coefficient) values (see Figure 10), all variables (LAI, K_c, and K_{cb}) show a noticeable decrease at the start and end of each year, except for K_e, which rises. This increase in soil evaporation is significant, as the soil is largely free of weeds during these periods, leading to greater water loss and increased dryness. Clearly, as pointed out by the IPCC Grupo Intergubernamental de Expertos sobre Cambio Climático (IPCC) - Junta de Andalucía - Consejería de Sostenibilidad' Medio Ambiente y Economía Azul. (2022), climate change is a key driver of

rising air temperatures. As climate change progresses into global warming, it logically leads to higher temperatures and, consequently, an increase in the soil evaporation coefficient.

This work offers detailed insights by linking temporal behavior and soil dryness during a critical phenological stage for citrus orchards, using a large number of images over an extended period. To investigate soil dryness, especially in the last fortnight of August 2021 and 2022, when the highest-quality orange harvest occurs, Weibull curves, a suitable fit for backscatter data distribution, were automatically computed (Figures 16, 20, and 21) to analyze drought events of these specific periods. In this case, greater distances between matching points in different point clouds correspond to higher Weibull values, indicating increased soil dryness. This matches 30–40% of citrus plots harvested in August within the El Hundido irrigators' community, which aligns with the percentage of distance on the Weibull distribution's abscissa. The analysis concludes that August 2022 was 12% drier than August 2021, August 2021 was 4% drier than the full 2021–2022 period, making August 2022 overall 16% drier than the full-time range.

Similarly, analyses of satellite image pixel intensity by DN distribution (Figures 12, 15, and 19) reveal a notable finding: the peak percentage of points corresponds to 4% of citrus plots in the study area irrigated by drip (10.8 ha out of 270 ha).

Integrating Sentinel-1 data with quantitative models to identify dryness and estimate water needs in citrus orchards presents significant improvement opportunities. Citrus orchard modeling has evolved from theory to a key part of decision support systems at multiple spatial scales, enabling further progress (Dela Torre et al., 2021). This evolution parallels rapid advances in remote sensing and SAR technology, driven by more frequent satellite data and the anticipated growth of drone-based SAR for precision agriculture.

5. Conclusions

This study evaluated the new CARP-Flux model, which uses Sentinel-1 images, backscatter data segmentation, and radar point cloud analysis. It was applied to an irrigator community in the Vega del Guadalquivir, a major citrus-growing region. Notably, the model improves water need estimates where the Hargreaves method underestimates by about 15%, particularly in irrigated or moist soils. This underestimation occurs because Hargreaves does not account for additional water availability or soil moisture, leading to lower ET_0 estimates when evapotranspiration is high.

Developing the model required using evolutionary algorithms, a tool of enormous interest not only in remote sensing but also, among other examples, in areas related to pollutants' diffusion in the environment (Ramírez-Juidías et al., 2015).

Apart from the new model for calculating water requirements in citrus orchards, the use of advanced statistical techniques, such as the Weibull distribution, has been particularly relevant in this work. This is due to their enormous potential for identifying study area use changes. For this reason, they are of particular interest along with the use of radar images, especially because of their practical complementarity.

It should be noted that the methodology used in this research can be applied to greater areas, such as large cities or entire countries. In this respect, future lines of work will consist of the compilation and analysis of 3D radar data in agricultural macro-areas with the aim of inferring their effect on the climatic comfort of large urban agglomerations. It should not be forgotten that in this type of study, it is essential to carry out supervised classification through the confusion matrix of fieldwork data in order to avoid false positives or negatives. For this reason, fieldwork plays an important role.

Author contributions

CRediT: **Emilio-José Cabello-Franco**: Conceptualization, Data curation, Formal analysis, Investigation, Methodology, Resources, Software, Validation, Visualization, Writing – original draft, Writing – review & editing; **Daniel Antón**: Conceptualization, Data curation, Formal analysis, Funding acquisition, Investigation, Methodology, Project administration, Resources, Software, Supervision, Validation, Visualization, Writing – original draft, Writing – review & editing; **Emilio Ramírez-Juidias**: Conceptualization, Data curation, Formal analysis, Funding acquisition, Investigation, Methodology, Project administration, Resources, Software, Supervision, Validation, Visualization, Writing – original draft, Writing – review & editing; **Francisco Perea-Torres**: Conceptualization, Data curation, Formal analysis, Investigation, Methodology, Project administration, Resources, Software, Supervision, Validation, Visualization, Writing – original draft, Writing – review & editing.

Disclosure statement

No potential conflict of interest was reported by the author(s).

Funding

About the authors

Emilio-José Cabello-Franco, Emerging researcher. Research Fellow at RSV3 Remote Sensing S.L. Doctoral student at Universidad de Sevilla. His primary research interest lies in applied environmental remote sensing.

Daniel Antón, Post-doctoral Research Fellow at Universidad de Sevilla. Research interests include 3D data generation from remote sensing imagery for diverse applications, and the reconstruction and analysis of heritage assets, with a focus on automated three-dimensional spatial approaches.

Emilio Ramírez-Juidias, Senior lecturer. Instituto Universitario de Arquitectura y Ciencias de la Construcción (IUACC) at Universidad de Sevilla. His primary research interest lies in applied environmental remote sensing. He specializes in applied environmental remote sensing.

Francisco Perea-Torres, Researcher at the Andalusian Institute of Agricultural and Fisheries Research and Training (IFAPA) (Center Las Torres) on the topic of crop irrigation.

ORCID

Emilio-José Cabello-Franco 🆔 http://orcid.org/0009-0003-2166-165X
Daniel Antón 🆔 http://orcid.org/0000-0002-4267-2433
Emilio Ramírez-Juidias 🆔 http://orcid.org/0000-0002-5861-7949
Francisco Perea-Torres 🆔 http://orcid.org/0000-0003-2907-8496

Data availability statement

The authors confirm that the data supporting the findings of this study are available within the article. In addition, the data that support the findings of this study are available from the corresponding author, DA, upon reasonable request.

References

Adrian, J., Sagan, V., & Maimaitijiang, M. (2021). Sentinel SAR-optical fusion for crop type mapping using deep learning and Google Earth Engine. *ISPRS Journal of Photogrammetry and Remote Sensing*, *175*, 215–235. https://doi.org/10.1016/j.isprsjprs.2021.02.018

Allen, R. G., & Pereira, L. S. (2009). Estimating crop coefficients from fraction of ground cover and height. *Irrigation Science*, *28*(1), 17–34. https://doi.org/10.1007/s00271-009-0182-z

Allen, R. G., Pereira, L. S., Raes, D., & Smith, M. (1998). Crop Evapotranspiration: Guidelines for Computing Crop Water Requirements; FAO Irrigation and Drainage Paper No. 56. FAO - Food and Agriculture Organization of the United Nations, Rome.

Allen, R. G., Tasumi, M., & Trezza, R. (2007a). Satellite-based energy balance for mapping evapotranspiration with internalized calibration (METRIC)—model. *Journal of Irrigation and Drainage Engineering*, *133*(4), 380–394. https://doi.org/10.1061/(ASCE)0733-9437(2007)133:4(380)

Allen, R. G., Wright, J. L., Pruitt, W. O., Pereira, L. S., & Jensen, M. E. (2007b). Chapter 8. Water Requirements. In Glenn J. Hoffman, Robert G. Evans, Marvin E. Jensen, Derrel L. Martin, Ronald L. Elliott. (2nd Edn., pp. 208–288). American Society of Agricultural and Biological Engineers. https://doi.org/10.13031/2013.23691

Antón, D., & Amaro-Mellado, J.-L. (2021). Engineering graphics for thermal assessment: 3D thermal data visualisation based on infrared thermography, GIS and 3D point cloud processing software. *Symmetry* , *13*(2), 335. https://doi.org/10.3390/sym13020335

Antón, D., Carretero-Ayuso, M. J., Moyano-Campos, J., & Nieto-Julián, J. E. (2022). Laser scanning intensity fingerprint: 3D visualisation and analysis of building surface deficiencies. In Bienvenido-Huertas, D., Moyano-Campos, J. (Eds.), *New Technologies in Building and Construction*. (pp. 207–223). Springer Nature Singapore. https://doi.org/10.1007/978-981-19-1894-0_12

Bastiaanssen, W. G. M., Menenti, M., Feddes, R. A., & Holtslag, A. A. M. (1998). A remote sensing surface energy balance algorithm for land (SEBAL). 1. Formulation. *Journal of Hydrology*, 212–213, 198–212. https://doi.org/10.1016/S0022-1694(98)00253-4

Bhatti, M. T., Gilani, H., Ashraf, M., Iqbal, M. S., & Munir, S. (2024). Field validation of NDVI to identify crop phenological signatures. *Precision Agriculture*, 25(5), 2245–2270. https://doi.org/10.1007/s11119-024-10165-6

Climate Data. (2024). Climate data for cities worldwide. [WWW Document]. URL https://en.climate-data.org/ (accessed 7.10.24).

Dari, J., Brocca, L., Quintana-Seguí, P., Escorihuela, M. J., Stefan, V., & Morbidelli, R. (2020). Exploiting high-resolution remote sensing soil moisture to estimate irrigation water amounts over a mediterranean region. *Remote Sensing*, 12(16), 2593. https://doi.org/10.3390/rs12162593

De Michele, C., Kotsopoulos, S., & Calera Belmonte, A. (2020). EO Methodology for DIANA services: Earth Observation data products and services. [WWW Document]. URL https://diana-h2020.eu/wp-content/uploads/D2.1.pdf (accessed 7.8.24).

Dela Torre, D. M. G., Gao, J., & Macinnis-Ng, C. (2021). Remote sensing-based estimation of rice yields using various models: A critical review. *Geo-Spatial Information Science*, 24(4), 580–603. https://doi.org/10.1080/10095020.2021.1936656

Doorenbos, J., & Pruitt, W. O. (Eds.). (1977). Guidelines for predicting crop water requirements. *FAO Irrigation and drainage paper No. 24*. FAO - Food and Agriculture Organization of the United Nations.

El Hajj, M. M., Johansen, K., Almashharawi, S. K., & McCabe, M. F. (2023). Water uptake rates over olive orchards using Sentinel-1 synthetic aperture radar data. *Agricultural Water Management*, 288, 108462. https://doi.org/10.1016/j.agwat.2023.108462

Ellis, E. A., Allen, G. H., Riggs, R. M., Gao, H., Li, Y., & Carey, C. C. (2024). Bridging the divide between inland water quantity and quality with satellite remote sensing: An interdisciplinary review. *WIREs Water*, 11(4), e1725. https://doi.org/10.1002/wat2.1725

EOS Data Analytics. (2024). Crop Monitoring. [WWW Document]. Products. URL https://eos.com/products/crop-monitoring/ (accessed 6.1.24).

European Space Agency (ESA). (2024a). Overview of Sentinel-1 Mission [WWW Document]. Copernicus Program. Mission Oper. URL https://www.esa.int/Enabling_Support/Operations/Sentinel-1_operations (accessed 7.5.24).

European Space Agency (ESA). (2024b). Overview of Sentinel-2 Mission [WWW Document]. Copernicus Program. Mission Oper. URL https://www.esa.int/Enabling_Support/Operations/Sentinel-2_operations (accessed 7.5.24).

European Space Agency (ESA). (2024c). Copernicus Browser [WWW Document]. Copernicus Data Sp. Ecosyst. URL https://dataspace.copernicus.eu/browser/ (accessed 6.8.24).

Fernández Cacho, S., Fernández Salinas, V. M., Hernández León, E., López Martín, E., Quintero-Morón, V., Rodrigo Cámara, J. M., & Zarza Balluguera, D. (2010). *Paisajes y patrimonio cultural en Andalucía: Tiempo, usos e imágenes (v.II), PH cuadernos 27*. Consejería de Cultura, Instituto Andaluz del Patrimonio Histórico.

Food and Agriculture Organization of the United Nations (FAO). (2024). *Water use efficiency and water productivity within sustainability boundaries for resilient transformation of agrifood systems in NENA, in: FAO Regional Conference for the Near East (NERC)*. (pp. 1–10) FAO - Food and Agriculture Organization of the United Nations.

Frau Orynbaikyzy, A. (2023). *Crop type classification using the combination of Sentinel-1 and Sentinel-2 data*. Die Martin-Luther-Universität Halle-Wittenberg.

Friedman, S. P. (2024). A simple method for evaluating the relative water uptake rate of drip-irrigated crops. *Irrigation and Drainage*, 73(4), 1231–1245. https://doi.org/10.1002/ird.2956

Girardeau-Montaut, D. (2016). *CloudCompare: 3D point cloud and mesh processing software*. Open Source Proj.

Grupo Intergubernamental de Expertos sobre Cambio Climático (IPCC) - Junta de Andalucía - Consejería de Sostenibilidad' Medio Ambiente y Economía Azul.. (2022). Análisis de la evolución futura bajo Escenarios de Cambio Climático de las variables Climáticas y de las variables Derivadas. [WWW Document]. Escenarios locales de cambio climático. URL https://www.juntadeandalucia.es/medioambiente/portal/areas-tematicas/cambio-climatico-y-clima/escenarios-locales-de-cambio-climatico/escenarios-locales-de-cambio-climatico-actualizados-6-informe-ipcc (accessed 7.10.24).

Gupta, N. (2020). Using the Santa Fe Ant trail benchmarking problem to optimize genetic algorithms. *International Journal of High School Research*, 2(2), 12–16. https://doi.org/10.36838/v2i2.4

Hayat, F., Li, J., Iqbal, S., Peng, Y., Hong, L., Balal, R. M., Khan, M. N., Nawaz, M. A., Khan, U., Farhan, M. A., Li, C., Song, W., Tu, P., & Chen, J. (2022). A mini review of citrus rootstocks and their role in high-density orchards. 11(21), 2876. https://doi.org/10.3390/plants11212876

Jovanovic, N., Pereira, L. S., Paredes, P., Pôças, I., Cantore, V., & Todorovic, M. (2020). A review of strategies, methods and technologies to reduce non-beneficial consumptive water use on farms considering the FAO56 methods. *Agricultural Water Management*, 239, 106267. https://doi.org/10.1016/j.agwat.2020.106267

Komisarenko, V., Voormansik, K., Elshawi, R., & Sakr, S. (2022). Exploiting time series of Sentinel-1 and Sentinel-2 to detect grassland mowing events using deep learning with reject region. *Scientific Reports*, 12(1), 983. https://doi.org/10.1038/s41598-022-04932-6

Kpienbaareh, D., Sun, X., Wang, J., Luginaah, I., Bezner Kerr, R., Lupafya, E., & Dakishoni, L. (2021). Crop type and land cover mapping in northern Malawi using the integration of Sentinel-1, Sentinel-2, and PlanetScope satellite data. *Remote Sensing*, *13*(4), 700. https://doi.org/10.3390/rs13040700

MacDonald' Dettwiler and Associates Ltd (MDA). (2011). *Sentinel-1 product definition; Ref: S1-RS-MDA-52-7440*.

Martínez-Casasnovas, J. A., & Bordes, X. (2005). Viticultura de precisión: Predicción de cosecha a partir de variables del cultivo e índices de vegetación. *Rev. Teledetección*, *24*, 67–71.

Ministerio para la Transición Ecológica y el Reto Demográfico. (2024). Visor de Escenarios de Cambio Climático. [WWW Document]. AdapteCCa. URL https://escenarios.adaptecca.es/ (accessed 6.1.24).

Navarro, A., Rolim, J., Miguel, I., Catalão, J., Silva, J., Painho, M., & Vekerdy, Z. (2016). Crop monitoring based on SPOT-5 Take-5 and sentinel-1A data for the estimation of crop water requirements. *Remote Sensing*, *8*(6), 525. https://doi.org/10.3390/rs8060525

Osann Jochum, M. A. (2006). Operational space-assisted irrigation advisory services: Overview of and lessons learned from the project Demeter. In D'Urso, G., Osann Jochum, M.A., Moreno, J. (Eds.), *AIP Conference Proceedings*. (pp. 3–13). American Institute of Physics. https://doi.org/10.1063/1.2349322

Osco, L. P., Wu, Q., de Lemos, E. L., Gonçalves, W. N., Ramos, A. P. M., Li, J., & Marcato, J. (2023). The Segment Anything Model (SAM) for remote sensing applications: From zero to one shot. *International Journal of Applied Earth Observation and Geoinformation*, *124*, 103540. https://doi.org/10.1016/j.jag.2023.103540

Pereira, L. S., & Allen, R. G. (1999). Crop water requirements. In Van Lier, H., Pereira, L.S., Steiner, F. (Eds.), *CIGR Handbook of Agricultural Engineering*. (Vol. 1, pp. 213–262). Land and Water Engineering. American Society of Agricultural Engineers.

Pereira, L. S., Paredes, P., Melton, F., Johnson, L., Wang, T., López-Urrea, R., Cancela, J. J., & Allen, R. G. (2020). Prediction of crop coefficients from fraction of ground cover and height. Background and validation using ground and remote sensing data. *Agricultural Water Management*, *241*, 106197. https://doi.org/10.1016/j.agwat.2020.106197

Pereira, L. S., Paredes, P., Oliveira, C. M., Montoya, F., López-Urrea, R., & Salman, M. (2024). Single and basal crop coefficients for estimation of water use of tree and vine woody crops with consideration of fraction of ground cover, height, and training system for Mediterranean and warm temperate fruit and leaf crops. *Irrigation Science*, *42*(6), 1019–1058. https://doi.org/10.1007/s00271-023-00901-7

Pérez-Pérez, J. G., Quiñones, A., & Bonet, L. (2020). Nuevos retos para el riego y la fertilización en cítricos. In García-Álvarez-Coque, J., Moltó, E. (Eds.), *Una hoja de ruta para la citricultura española* (1 ed., pp. 215–225). Almeria, Spain; Cajamar Caja rural.

Pôças, I., Calera, A., Campos, I., & Cunha, M. (2020). Remote sensing for estimating and mapping single and basal crop coefficientes: A review on spectral vegetation indices approaches. *Agricultural Water Management*, *233*, 106081. https://doi.org/10.1016/j.agwat.2020.106081

Ramírez-Juidías, E. (2022). A mini-review of remote sensing applied to salt-marshes. *Acad. Lett*. Article 4662. https://doi.org/10.20935/AL4662

Ramírez-Juidias, E., Amaro-Mellado, J.-L., Leiva-Piedra, J. L., & Mediano-Guisado, J. A. (2024). Use of remote sensing techniques to infer the red globe grape variety in the Chancay-Lambayeque valley (Northern Peru). *Remote Sensing Applications: Society and Environment*, *33*, 101108. https://doi.org/10.1016/j.rsase.2023.101108

Ramírez-Juidías, E., & José Cabello-Franco, E. (2023). New remote sensing technologies applied to the prediction of spontaneous forest fires., In Mokhtari, M. (Ed.), *Natural Hazards - New Insights*. Rijeka: Intech Open. https://doi.org/10.5772/intechopen.110501; ISBN 978-1-80355-849-3.

Ramírez-Juidías, E., Pozo-Morales, L., & Galán-Ortiz, L. (2015). Procedimiento para la Obtención de una Imagen Teledetectada a Partir de Fotografía. *Es2537783b2 (Wo2014198974)*,

Sahaar, S. A., Niemann, J. D., & Elhaddad, A. (2022). Using regional characteristics to improve uncalibrated estimation of rootzone soil moisture from optical/thermal remote-sensing. *Remote Sensing of Environment*, *273*, 112982. https://doi.org/10.1016/j.rse.2022.112982

Salgado, R., & Mateos, L. (2021). Evaluation of different methods of estimating ET for the performance assessment of irrigation schemes. *Agricultural Water Management*, *243*, 106450. https://doi.org/10.1016/j.agwat.2020.106450

Seminara, S., Bennici, S., Di Guardo, M., Caruso, M., Gentile, A., La Malfa, S., & Distefano, G. (2023). Sweet orange: Evolution, characterization, varieties, and breeding perspectives. *Agriculture*, *13*(2), 264. https://doi.org/10.3390/agriculture13020264

Shrestha, B., Stephen, H., & Ahmad, S. (2021). Impervious surfaces mapping at city scale by fusion of radar and optical data through a random forest classifier. *Remote Sensing*, *13*(15), 3040. https://doi.org/10.3390/rs13153040

Singh, J., Sharma, V., Pandey, K., Ahmed, S., Kaur, M., & Singh Sidhu, G. (2021). *Horticultural Classification of Citrus Cultivars, in: Citrus - Research, Development and Biotechnology*. IntechOpen. https://doi.org/10.5772/intechopen.96243

Steduto, P., Hsiao, T. C., Fereres, E., & Raes, D. (Eds.). (2012). Respuesta del rendimiento de los cultivos al agua. In *Estudio FAO: Riego y Drenaje*. (pp. 1–530). FAO - Food and Agriculture Organization of the United Nations. ISSN 0254–5284

Tenreiro, T. R., García-Vila, M., Gómez, J. A., Jiménez-Berni, J. A., & Fereres, E. (2021). Using NDVI for the assessment of canopy cover in agricultural crops within modelling research. *Computers and Electronics in Agriculture*, *182*, 106038. https://doi.org/10.1016/j.compag.2021.106038

Tong, J., Wu, L., Li, B., Jiang, N., Huang, J., Wu, D., Zhou, L., Yang, Q., Jiao, Y., Chen, J., Zhao, K., & Pei, X. (2024). Image-based vegetation analysis of desertified area by using a combination of ImageJ and photoshop software. *Environmental Monitoring and Assessment*, *196*(3), 306. https://doi.org/10.1007/s10661-024-12479-4

Tufail, R., Ahmad, A., Javed, M. A., & Ahmad, S. R. (2022). A machine learning approach for accurate crop type mapping using combined SAR and optical time series data. *Advances in Space Research*, *69*(1), 331–346. https://doi.org/10.1016/j.asr.2021.09.019

Vidican, R., Mălinaș, A., Ranta, O., Moldovan, C., Marian, O., Ghețe, A., Ghișe, C. R., Popovici, F., & Cătunescu, G. M. (2023). Using remote sensing vegetation indices for the discrimination and monitoring of agricultural crops: A critical review. *Agronomy*, *13*(12), 3040. https://doi.org/10.3390/agronomy13123040

Zhao, Q., Xie, Q., Peng, X., Lai, K., Wang, J., Fu, H., Zhu, J., & Song, Y. (2024). Understanding the temporal dynamics of coherence and backscattering using sentinel-1 imagery for crop-type Mapping. *IEEE Journal of Selected Topics in Applied Earth Observations and Remote Sensing*, *17*, 6875–6893. https://doi.org/10.1109/JSTARS.2024.3373489